Review Article

Open Access

Xiaoxiao Xue*, Minghao Qi, and Andrew M. Weiner

Normal-dispersion microresonator Kerr frequency combs

Abstract: Optical microresonator-based Kerr frequency comb generation has developed into a hot research area in the past decade. Microresonator combs are promising for portable applications due to their potential for chip-level integration and low power consumption. According to the group velocity dispersion of the microresonator employed, research in this field may be classified into two categories: the anomalous dispersion regime and the normal dispersion regime. In this paper, we discuss the physics of Kerr comb generation in the normal dispersion regime and review recent experimental advances. The potential advantages and future directions of normal dispersion combs are also discussed.

Keywords: frequency comb; microresonator; Kerr effect; four-wave mixing; group velocity dispersion; mode coupling; modulational instability; dark soliton; thermo-optic effect; pulse shaping; mode-locking

1 Introduction

Optical frequency combs are broadband light sources that contain a series of equally spaced, phase-locked frequency components [1]. They are widely employed in many applications, including optical frequency metrology [2, 3], high-resolution spectroscopy [4], microwave photonic signal generation/processing [5–8], and fiber telecommunications [9–11]. Conventionally, optical frequency combs are generated with mode-locked lasers [1, 12] or electro-

optic modulators [13]. These systems are usually built with discrete optical components and have a large volume and high complexity. Naturally, there is strong motivation to implement ultra-compact integrated comb sources that are suitable for on-chip and portable applications. In this article, we discuss one highly promising approach, the microresonator-based Kerr frequency comb generation [14], often termed microcombs or Kerr combs. The basic scheme of Kerr comb generation is illustrated in Figure 1. The key component here is an optical microresonator made of $\chi^{(3)}$ nonlinear materials and having a high quality factor (Q). A single-frequency continuous-wave (cw) laser with moderate power is coupled into the microresonator; aided by the strong resonant enhancement of the intracavity power, the single-frequency input is converted to a broadband frequency comb through nonlinear wave mixing.

Hyperparametric oscillation (in fibers also named modulational instability) in high-Q microcavities driven by a cw pump laser was first demonstrated in 2004 [15, 16]. Then in 2007, more sidebands were generated with an increased pump power forming a broadband comb, which was explained as cascaded four-wave mixing from a frequency domain perspective [17]. Intense studies have been performed since then. To date, a variety of materials and microresonator structures have been exploited for Kerr comb generation, including whisper-gallery mode (WGM) microresonators made of silica [17, 18], fused quartz [19], crystalline fluorides [20–22], and sapphire [23]; planar waveguide microrings made of Hydex glass [24], silicon nitride [25], aluminum nitride [26], diamond [27], and silicon [28]. Some of these are depicted in the inset of Figure 1. The line spacing of a microcomb is determined by the microresonator's free spectral range (FSR), which ranges from tens of GHz to THz. Owing to the ultra-high microresonator Q factors that can be achieved, microcombs may achieve very low power consumption. Pump threshold powers down to the sub-mW level have been demonstrated for silica microresonators with Q factors of 10^8– 10^9 [17]. Another outstanding feature of microcombs is that they can provide ultra-broad spectra. Octave-spanning comb generation from a single microresonator without any external broadening has been demonstrated [29, 30].

*Corresponding Author: Xiaoxiao Xue: School of Electrical and Computer Engineering, Purdue University, 465 Northwestern Avenue, West Lafayette, Indiana 47907-2035, USA, E-mail: xue40@purdue.edu
Minghao Qi, Andrew M. Weiner: School of Electrical and Computer Engineering, Purdue University, 465 Northwestern Avenue, West Lafayette, Indiana 47907-2035, USA
and Birck Nanotechnology Center, Purdue University, 1205 West State Street, West Lafayette, Indiana 47907, USA, E-mail: mqi@purdue.edu, amw@purdue.edu

This is especially valuable for the pursuit of *f-2f* self-referencing commonly employed to stabilize mode-locked laser combs for optical frequency metrology. Microcombs are now being extensively investigated due to their potential to bring revolutionary improvements to the frequency comb area.

One important aspect of microcomb researches focuses on the comb time-domain properties and mode-locking mechanisms [31–56]. It is now understood that Kerr comb generation can be divided into two stages: the first stage is hyperparametric oscillation related to the growth of new frequency components from an initial cavity that only contains the pump and some low-level noise; the second stage of frequency comb formation brings in rich nonlinear dynamics, including subcomb formation, chaos, breathing, and mode-locking transitions. The optical group velocity dispersion inside the microresonator plays an important role in both stages. It has long been known that nonlinear propagation of a single wave in dispersive single-mode optical fibers exhibits modulational instability only if the group velocity dispersion is anomalous (additional possibilities are available if the wave is allowed to interact with a second, distinguishable wave through cross-phase modulation) [57]. Although this condition is relaxed in cavities [58, 59], most research on comb generation has employed microresonators with anomalous dispersion [17, 18, 21–30, 33–39], because the phase matching condition for hyperparametric oscillation remains easier to satisfy in this regime. Broadband phase-locked Kerr combs have been demonstrated in the second stage via subcomb offset frequency matching [33], ultrashort pulse generation [35], bright soliton formation [36], and self-injection locking [37]. Kerr comb generation in normal dispersion microresonators has also been demonstrated [31, 40–48], but has been less explored. Although achieving modulational instability for comb initiation in the general normal dispersion regime is more difficult, comb generation using normal dispersion microresonators also offers potential advantages. It relaxes the requirement for dispersion engineering of the waveguide that sometimes causes reduced microresonator Q factors and higher power consumption in comb generation. This is especially valuable for comb generation in the visible wavelength range where the material dispersion is strongly normal and for which it is therefore more challenging to get anomalous dispersion through dispersion engineering. There are also indications that normal dispersion combs may admit more deterministic approaches to mode-locking [46] and offer potential for better power efficiency [55]. From a scientific perspective, normal dispersion combs may exhibit behavior distinct to that observed

with anomalous dispersion combs, providing new opportunities for studies of nonlinear cavity dynamics.
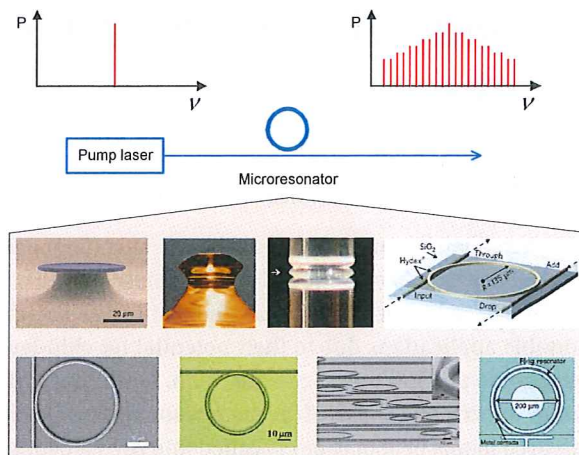

Figure 1: Optical microresonator-based Kerr frequency comb generation. A single pump frequency is converted into a broadband frequency comb by using a high-Q nonlinear microresonator. The inset shows different materials and structures that have been employed for Kerr comb generation. From top left to bottom right: silica microtoroid [17], fluoride crystalline [22], fused quart [19], Hydex glass microring [24], silicon nitride microring [25], aluminum nitride microring [26], diamond microring [27], silicon microring [28].

It is instructive to recall that the interplay between nonlinear phase modulation and group velocity dispersion plays a decisive role in modern passively mode-locked lasers [60]. Mode-locking is possible in both anomalous and normal dispersion regimes but is accompanied by quite different behavior [61]. Cavities with net anomalous dispersion produce approximately bandwidth-limited pulses that closely resemble the solitons observed in anomalous dispersion fibers. Cavities with net normal dispersion produce pulses that are strong chirped; however, these pulses may be compressed to achieve transform-limited duration and pulse shape with dispersion compensation external to the cavity. Such chirped pulse operation offers advantages such as increased stability and pulse energy, especially in systems such as mode-locked fiber lasers [62, 63]. Although the details are different, similar contrasts come into play in comb generation with nonlinear microresonators.

In this article, we review both experimental research and the underlying physics of Kerr frequency comb generation in the normal-dispersion regime. Microresonator dispersion and engineering are briefly introduced in Section 2 to illustrate the opportunities for normal-dispersion Kerr combs. Corresponding to the two stages of comb genera-

tion, Section 3 discusses modulational instability in nonlinear dispersive cavities and discusses how mode interactions can aid in attainment of modulational instability in cavities that otherwise display global normal dispersion. Section 4 introduces time-domain investigations of normal-dispersion Kerr combs and their underlying mode-locking mechanisms. Spectral tuning with microheaters and programmable Kerr comb generation with coupled microresonators is described in Section 5. Finally, in Section 6, we discuss the future research directions for normal-dispersion Kerr combs.
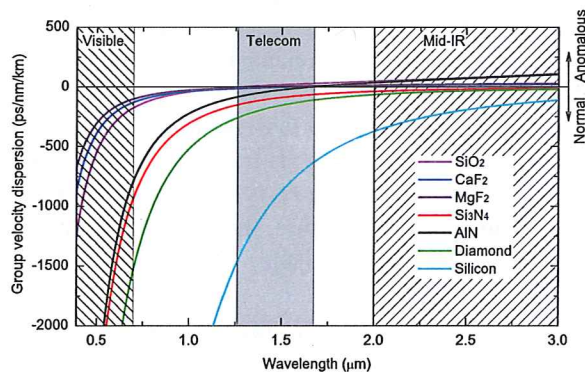

Figure 2: Group velocity dispersion (D parameter) of different materials that have been employed for Kerr comb generation. Plotted with the data from Ref. [66].

2 Microresonator group velocity dispersion

The group velocity dispersion of a waveguide is usually denoted as [60]

$$\beta_2 = \frac{d^2\beta}{d\omega^2} \tag{1}$$

where β is the propagation constant and ω is the angular frequency. Another frequently used parameter is called the dispersion parameter, denoted by D, which is the derivative of group delay per unit transmission length with respect to wavelength. The relation between β_2 and D is given by

$$D = -\frac{2\pi c}{\lambda^2}\beta_2 \tag{2}$$

where c is the speed of light in vacuum and λ is wavelength. The dispersion is said to be "normal" if $\beta_2 > 0$ ($D < 0$), and "anomalous" if $\beta_2 < 0$ ($D > 0$).

The group velocity dispersion is mainly composed of material and geometric dispersion. The geometric dispersion can be further divided into the dispersion related to the waveguide cross-section and the dispersion induced by the microresonator curvature [64, 65]. Figure 2 shows the material dispersion in a wide wavelength range for several materials that have been exploited for Kerr comb generation [66]. In the lightwave C band (1.530–1.565 µm) where Kerr comb generation has been intensely investigated, the bulk materials of SiO_2 and MgF_2 have low anomalous dispersion while Si_3N_4, AlN, diamond and silicon have normal dispersion; the zero-dispersion wavelength of CaF_2 is in the C band so that there is both an anomalous and a normal dispersion region. Generally, material dispersion cannot be changed by a wide margin, so the overall dispersion is engineered mainly by tailoring the microresonator geometry. For WGM microresonators, dispersion engineering is performed by shaping the light-guiding boundary via micromachining [67]. For planar waveguide microresonators, dispersion engineering can be performed by changing the width and height of the waveguide cross-section [68], inserting slot layers [69], or conformal coating [70]. The difficulty level of different dispersion engineering methods varies in practical implementations. For planar waveguide microresonators, changing the waveguide cross-section dimension is generally the easiest to implement. Figure 3 shows examples of the dispersion calculated for Si_3N_4 waveguides [71]. By choosing the appropriate width and height of the waveguide, overall anomalous dispersion can be achieved in the telecom band. However, tailoring the dispersion does not always conform to other requirements that are also important for Kerr comb generation. For example, thick waveguides (generally >0.75 µm) are helpful to achieve anomalous dispersion for Si_3N_4, but suffer from increased susceptibility to cracking due to high stress, resulting in lower microresonator Q factors and higher power consumption in comb generation. In Figure 2, one notable wavelength range is the visible range, where all the materials depicted show strong normal dispersion. It is much more challenging to achieve anomalous dispersion in this range. Therefore, it is highly interesting to investigate Kerr comb generation in the normal dispersion regime.

3 Modulational instability in microresonators

Hyperparametric oscillation, which in fibers is also named modulational instability, refers to the initial stage of comb generation. Like any kind of oscillator, for new frequencies to form, there should be a mechanism of gain to overcome
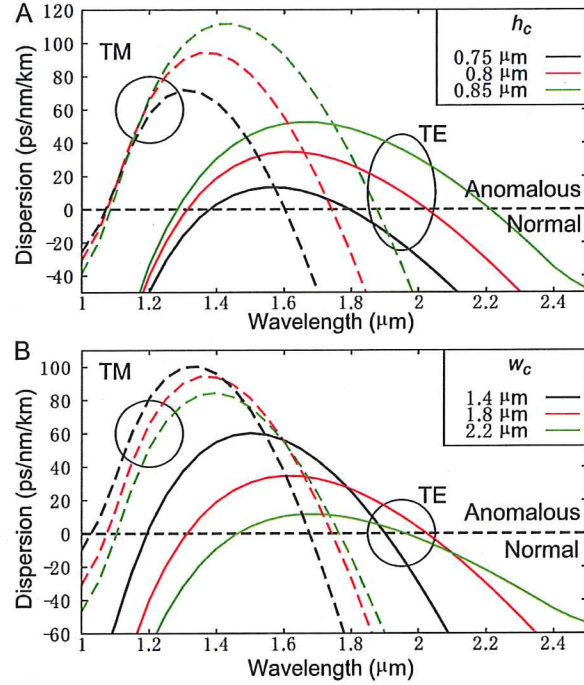
Figure 3: Dispersion engineering of Si_3N_4 waveguide embedded in SiO_2 by tailoring the waveguide cross-section. w_c and h_c represent the waveguide width and height, respectively. Simulated group velocity dispersion of the fundamental TE and TM modes when (A) $w_c = 1.8$ μm and $h_c = 0.75$ μm, 0.8 μm, and 0.85 μm; (B) $h_c = 0.8$ μm and $w_c = 1.4$ μm, 1.8 μm, and 2.2 μm. Adapted from Ref. [71].

the cavity loss. The parametric gain in Kerr comb generation is a consequence of external driving, dispersion and Kerr nonlinearity. Here we first summarize the basic analysis of cavity modulational instability and then discuss the impact of mode crossing and coupling.

3.1 Basic analysis based on mean-field Lugiato–Lefever equation

Early in the 1990s, Haelterman et al did the theoretical analysis for the temporal modulation instability in an externally driven nonlinear cavity [58]. Most of the results and conclusions that we will introduce in section 3.1 are taken from the paper of Haelterman et al [58]. Assuming the cavity round-trip length is much shorter than the dispersion length and the nonlinear length (which is generally the case for high-Q microresonators), the evolution of the intracavity optical complex field envelope obeys the

following mean-field Lugiato–Lefever (LL) equation [58]

$$t_R \frac{\partial E(t, \tau)}{\partial t} = \left[-\alpha - i\delta_0 - iL\frac{\beta_2}{2}\frac{\partial^2}{\partial \tau^2} + i\gamma L |E|^2 \right] E + \sqrt{\theta}E_{in}$$
(3)

Here, t_R and L are the cavity round-trip time and length, respectively; τ is fast time related to the cavity azimuthal position θ by $\tau = \theta R/v_g$ where R is the cavity radius and v_g is the group velocity; t is the slow time related to the number of round-trips (m) that the light transmits in the cavity, given by $t = mt_R$; α is the round-trip loss including both intrinsic and external coupling-induced loss; δ_0 is phase detuning of the pump laser, related to frequency detuning by $\delta_0 = (\omega_0 - \omega_p) t_R$ where ω_0 and ω_p are cavity resonant frequency and pump frequency, respectively; β_2 is the second-order dispersion (i.e. group velocity dispersion), with higher-order dispersion terms neglected; γ is the Kerr coefficient; θ is the fraction of power lost per round trip due to coupling; E_{in} is external driving field.

In much of the literature, the following normalized form is used for simplicity [58].

$$\frac{\partial F(t', \tau')}{\partial t'} = \left[-1 - i\Delta - i\eta\frac{\partial^2}{\partial \tau'^2} + i|F|^2 \right] F + S$$
(4)

The normalization is performed with $t' = \alpha t/t_R$, $\tau' = \tau\sqrt{2\alpha/(|\beta_2| L)}$, $F = E\sqrt{\gamma L/\alpha}$, $S = E_{in}\sqrt{\gamma L\theta/\alpha^3}$, $\Delta = \delta_0/\alpha$, and $\eta = \text{sign}(\beta_2)$.

Equations (3) and (4) are also known as the externally driven nonlinear Schrödinger equation. Compared with the ordinary nonlinear Schrödinger equation in fibers [57], the main difference of the LL equation is the presence of a driving term with detuning. As we introduced earlier, it is well known that modulational instability in single-mode fibers requires anomalous dispersion (i.e. $\eta = -1$) [57]. In comparison, modulation instability in cavities is affected by the cavity boundary condition and may arise in both anomalous and normal dispersion regimes [58, 59]. The analysis of modulational instability can be performed by adding a small perturbation term with a certain frequency in fast time (i.e. $\exp(i\Omega\tau')$ where Ω is the perturbation angular frequency) to the stationary cw solution and investigate how the perturbation amplitude will evolve with slow time. Using the normalized equation, the cavity modulational instability gain is given by

$$g = -1 + \sqrt{4Y(\Delta - \eta\Omega^2) - (\Delta - \eta\Omega^2)^2 - 3Y^2}$$
(5)

where $Y = |F|^2$ the stationary intracavity pump power. With properly selected parameters, g can be a real positive number and the perturbation amplitude increases exponentially as $\exp(gt')$. Note that in Equation (5) the phase

detuning and the dispersion-induced phase term come together as a single phase term, which implies that the effect of dispersion can be altered by changing the phase detuning. Actually, for a given intracavity power, if we choose the phase detuning in the different dispersion regimes to satisfy $\Delta_{\eta=-1}+\Delta_{\eta=1} = 4Y$, the modulational instability gain spectra will be exactly the same for the anomalous and normal dispersion regimes (see Figure 3 of Ref. [58]). The maximum gain and the corresponding frequency are given by

$$g_{max} = Y - 1 \tag{6}$$

$$\Omega_{max} = \sqrt{\eta\,(\Delta - 2Y)} \tag{7}$$

where Ω_{max} has units of inverse normalized fast time. For a given pumping condition (i.e. Y and Δ), hyperparametric oscillation requires that there be a frequency region in which the gain is real and positive. In the anomalous dispersion region ($\eta = -1$), it requires the following condition to be satisfied

$$Y > 1, \quad \text{for } \Delta \le 2 \tag{8a}$$

$$Y > \Delta/2, \quad \text{for } \Delta > 2 \tag{8b}$$

In the normal dispersion regime ($\eta = 1$), it requires

$$1 < Y < \Delta/2, \quad \text{with } \Delta > 2 \tag{9}$$

Now let us consider the input pump field. By setting the left side of Equation (4) to zero, we can get the relation between the input pump power ($X = |S|^2$) and the stationary intracavity pump power as follows:

$$X = Y^3 - 2\Delta Y^2 + \left(\Delta^2 + 1\right) Y \tag{10}$$

When $\Delta > \sqrt{3}$, the plot of Equation (10) has a typical S-shape. The S-curve can be divided into upper, middle, and lower branches separated by the inflection points, see Figure 4. The middle branch is unstable to cw perturbations (meaning that it is nearly impossible to access in experiments), while the upper and lower branches are cw stable. For different dispersion regimes, modulational instability occurs in different regions of the bistability curve. When the dispersion is anomalous, Equation (8a) corresponds to the upper branch, the middle branch and part of the lower branch; Equation (8b) corresponds to the upper and middle branches only. When the dispersion is normal, Equation (9) corresponds to a small region of the lower and middle branches near the inflection point.

The cavity boundary condition-induced modulational instability in the normal dispersion regime has been observed in fiber cavities [59, 72]. Although theoretically it
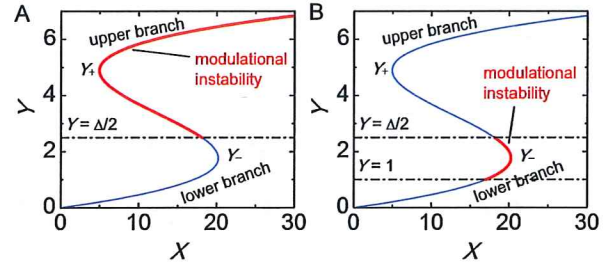

Figure 4: Modulation instability regions on the bistability curve for (A) anomalous dispersion and (B) normal dispersion. The phase detuning is $\Delta = 5$. The two inflection points are given by $Y_\pm = [2\Delta \pm (\Delta^2 - 3)^{1/2}]/3$. The upper and lower branches are stable to cw perturbations while the middle branch between $Y_\pm$ is cw unstable.

can be employed for comb generation in normal dispersion microresonators, the experimental implementation is difficult due to the strong thermal frequency shifts exhibited by microresonators when they are pumped under high power. When the pump laser wavelength is tuned into the resonance, the microresonator temperature increases; thus, in most materials, the resonance shifts to longer wavelength (red shift) due to thermal expansion and the thermo-optic effect [73] (note that some materials, e.g. CaF_2, BaF_2, crystalline quartz, have negative thermo-optic coefficient (i.e. $dn/dT < 0$) and hence display different thermal shifting behavior [74]). The Kerr effect also causes the resonances to shift in the red direction. To overcome the shifting of the resonances in the red direction, the pump laser needs to be tuned from shorter wavelength to longer wavelength (corresponding to continuously increasing the phase detuning with the sign convention employed in the LL equation, starting from a large negative value of phase detuning). In this process, the intracavity pump power stays on the upper branch before it suddenly drops to the lower branch (see Figure 5 for an illustration). The modulational instability region cannot be reached. Although it might be possible to get to the modulational instability region by monitoring the effective detuning and controlling the pump laser power and wavelength accordingly, the lower branch is generally thermally unstable because the pump laser is effectively red detuned with respect to the resonance in this region [73] (i.e., the pump laser wavelength is longer than the resonant wavelength that is shifted due to the thermo-optic and Kerr effects). Although modulational instability is generally absent on the upper branch for normal dispersion microresonators, in the next section, we will see that modulational instability may occur on the upper branch with the help of mode crossing and coupling, which provides a more favorable approach for comb generation.
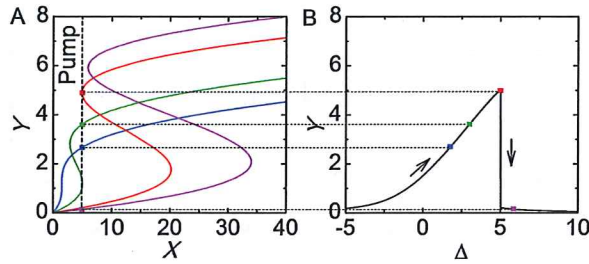
Figure 5: Illustration of the intracavity pump power when phase detuning is continuously increased. (A) Intracavity power versus input pump power (i.e. the bistability curve) for different phase detunings. (B) Intracavity power versus phase detuning for the fixed pump power (X) indicated by the dashed vertical line in (A). The intracavity power stays on the upper branch before it suddenly drops down to the lower branch. Adapted by permission from Macmillan Publishers Ltd: Nature Photonics [46], copyright 2015.

3.2 Impact of mode crossing and coupling

It is known that modulation instability may happen in normal dispersion fibers or waveguides when the optical field interacts with another field that has a different polarization or wavelength [75–77]. A similar phenomenon can also happen in microresonators. In general, microresonators may have multiple transverse and polarization modes. Although ideally orthogonal, these modes may be coupled to each other due to variations of the waveguide dimensions and refractive index. If we consider the linear transmission of two coupled transverse modes with the same polarization, the evolution of their intracavity fields obey the following equations [78]

$$\frac{dA_1}{dt} = \left[-\frac{1}{\tau_{o1}} - \frac{1}{\tau_{e1}} - i(\omega_1 - \omega_p) \right] A_1 + i\kappa_{12}A_2 + \sqrt{\frac{2}{\tau_{e1}}} E_{in} \tag{11}$$

$$\frac{dA_2}{dt} = \left[-\frac{1}{\tau_{o2}} - \frac{1}{\tau_{e2}} - i(\omega_2 - \omega_p) \right] A_2 + i\kappa_{21}A_1 + \sqrt{\frac{2}{\tau_{e2}}} E_{in} \tag{12}$$

where A_1 and A_2 are normalized field envelopes such that $|A_{1,2}|^2$ is equal to the energy in the respective modes integrated over the microresonator volume; $1/\tau_{o1}$ and $1/\tau_{o2}$ are decay rates due to the intrinsic loss; $1/\tau_{e1}$ and $1/\tau_{e2}$ are coupling rates between the resonator and the bus waveguide; ω_1, ω_2 and ω_p are the resonant frequencies of the two modes and the frequency of the input probe field, respectively; $\kappa_{12} = \kappa_{21}^* = \kappa$ is the coupling coefficient. Here we use the notation conformal to that usually used in coupled resonator analysis [78]. The relation with the notation in the LL equation are as follows: $A_{1,2} = E_{1,2}\sqrt{t_R}$, $1/\tau_{o1,2} + 1/\tau_{e1,2} = \alpha_{1,2}/t_R$, $1/\tau_{e1,2} = \theta/(2t_R)$. By setting the left sides of Equations

(11) and (12) to zero and solving, we can get the steady-state solution of the intracavity field. The microresonator transmission spectrum defined as the power at the through port divided by the input power is then calculated by $T = \left| E_{in} - A_1\sqrt{2/\tau_{e1}} - A_2\sqrt{2/\tau_{e2}} \right|^2 / |E_{in}|^2$. Figure 6 shows some simulated examples adapted from Ref. [45]. Without mode coupling ($\kappa = 0$), the two resonances approach and cross each other at a constant rate. In comparison, with mode coupling turned on ($\kappa \neq 0$), the two resonances shift from their nature frequencies, leading to an avoided crossing.

The mode coupling induced avoided mode crossing has been found unfavorable for comb generation in the anomalous dispersion regime, because it causes fluctuations of the comb spectrum [79] and may prevent solition mode-locking when strong mode coupling occurs close to the pump [38]. Nevertheless, in the normal dispersion regime, the relative positions of the resonances belonging to the same transverse mode may be altered by mode coupling such that they correspond to an equivalent anomalous dispersion. Modulational instability may thus occur on the upper branch of the bistability curve, which is generally impossible for normal dispersion microresonators in the case of no mode coupling (recall the discussion in the last section). This mode coupling induced modulational instability has been found to play a key role that enables comb generation in normal dispersion microresonators in experiments [40, 45–48].
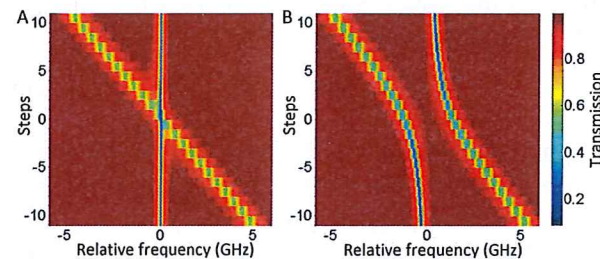

Figure 6: Simulated transmission of one resonator with two coupled modes. The first mode frequency is fixed while the second mode frequency moves across the first one. (A) Without mode coupling, $\kappa = 0$. (B) With mode coupling, $\kappa = i \cdot 8.25 \times 10^9 s^{-1}$. The other parameters are as follows: $\tau_{o1} = 2.79 \times 10^{-9}s$, $\tau_{e1} = 4.00 \times 10^{-9}s$, $\tau_{o2} = 5.78 \times 10^{-10}s$, $\tau_{e2} = 3.38 \times 10^{-9}s$. Adapted from Ref. [45].

Figure 7A shows one example of a Si_3N_4 microring resonator [45]. To fabricate the microresonator, an under cladding layer of 3 μm thermal oxide is grown on a silicon wafer in an oxidation tube at 1100°C. A 550 nm Si_3N_4 film is then deposited at 800°C on the oxidized wafer
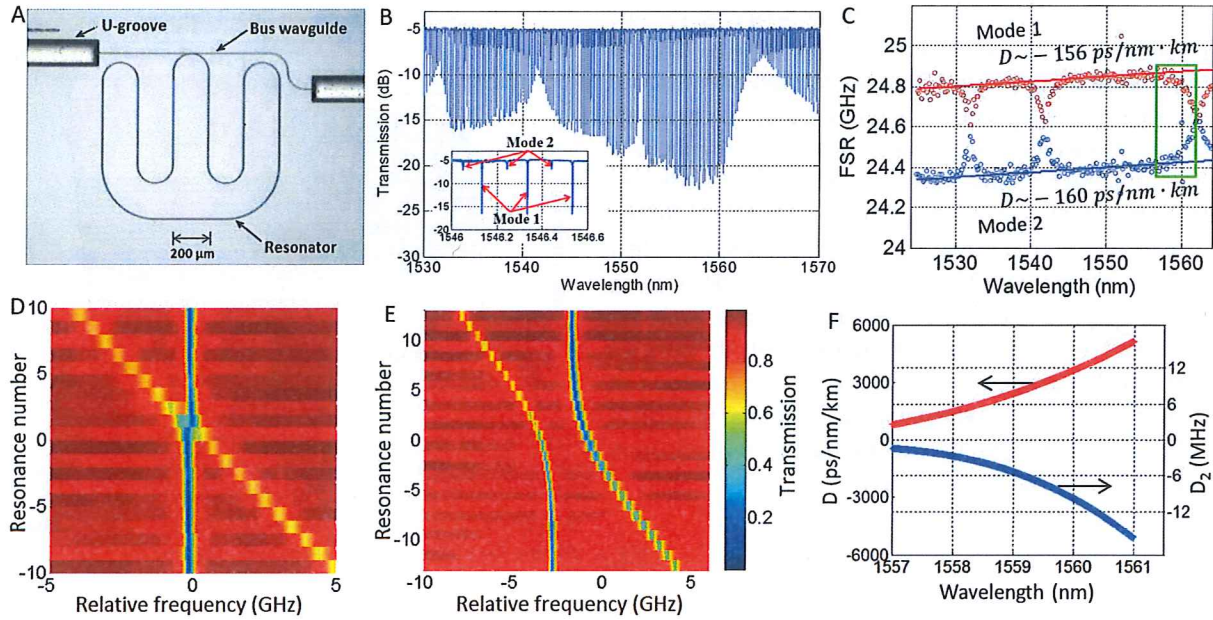
Figure 7: Experimental evidence of mode coupling in a Si_3N_4 microring resonator. (A) Microscope image of the microring. (B) Transmission spectrum. (C) FSR versus wavelength for the two modes. (D) Zoom-in view of the transmission in the region around 1552 nm, showing weak mode coupling. (E) Zoom-in view of the transmission in the region around 1562 nm, showing strong mode coupling. (F) Local dispersion retrieved from the FSR slope for mode 1 in the strong mode coupling region around 1562 nm (marked with a green box in (C)). Adapted from Ref. [45]. FSR: free spectral range.

using low-pressure chemical vapor depositions. A negative hydrogen silsesquioxane (HSQ) resist is used to pattern the waveguide and resonator via an electron-beam lithography system at 100 kV. After developing in tetramethylammonium hydroxide solution, the HSQ pattern is transferred to the Si_3N_4 film using reactive ion etching. Then, a 3.5 μm thick low temperature oxide film, which serves as an upper cladding, is deposited at 400°C followed by an annealing step undertaken at 1100°C in an N_2 atmosphere. The microring circumference shown in Figure 7A is 5.92 mm corresponding to a FSR of ~25 GHz. The width of the ring waveguide and the bus waveguide is 2 and 1 μm, respectively. (Most Si_3N_4 microrings discussed in the following parts of this paper have similar waveguide cross-section dimension unless explicitly mentioned.) The transmission spectrum of the microring measured in the lightwave C band is shown in Figure 7B. Two transverse modes can be observed from the zoom-in of transmission (inset). Figure 7C shows the resonance spacing (i.e. FSR) versus the wavelength, measured with frequency-comb-assisted spectroscopy [64]. Around the mode-crossing wavelengths 1532, 1542 and 1562 nm, the FSR slope is drastically changed due to mode coupling induced resonance shifts. Around another mode-crossing wavelength at 1552 nm, however, the slope of the FSR curves are only changed slightly, suggesting a wavelength

dependence of the mode coupling coefficient. Zoom-ins of the transmission in the mode-crossing regions around 1552 and 1562 nm are shown in Figures 7D and 7E, respectively. Here, the transmission spectrum is sliced into pieces separated by a constant 24.82 GHz increment (the nominal FSR of mode 1 around 1542 nm) and vertically aligned, resulting in pictures very similar to the simulated results as shown in Figure 6. Note that the mode coupling coefficient ($κ$) can be obtained by sweeping its value in the numerical simulations based on Eqs. (11) and (12) and comparing the simulated transmission spectrum with the experimentally measured results until the best match is obtained.

The local group velocity dispersion is related to the FSR variation by [33]

$$\beta_2 = -\frac{n_0 D_2}{c D_1^2} \qquad (13)$$

where $D_2 = \omega_{m+1} - \omega_m - (\omega_m - \omega_{m-1})$, ω_m is the resonant angular frequency and $D_2/(2\pi)$ denotes the difference in FSR for adjacent resonances; n_0 is the refractive index; c is light speed in vacuum; and $D_1 = 2\pi$FSR. The simulated dispersion parameter D, assuming no mode coupling, is -156 ps/nm/km and -160 ps/nm/km (which is in the normal dispersion regime) for the two modes, respectively. Figure 7F shows the local dispersion for mode 1 in the mode-crossing area around 1562 nm (marked with

a green box in Figure 7C). Due to mode coupling, the dispersion changes to anomalous and becomes as large as ~5000 ps/nm/km around 1561 nm. Comb generation is observed when the pump laser pumps the resonances in this area, as shown in Figure 8. In the test, the pump laser is tuned into each resonance from the blue side, thus the intracavity pump power stays on the upper branch of the bistability curve. The comb line spacing increases when the resonance pumped is further from the mode crossing wavelength (i.e., ~1562 nm). As a result, there is always one initial comb line pinned at approximately the position of the mode crossing. The comb line spacing corresponds to the frequency with maximum modulational instability gain. Using the un-normalized LL equation, the maximum gain frequency can be written as

$$\omega_{max} = \sqrt{\frac{2\left(\delta_0/L - 2\gamma P_s\right)}{\beta_2}} \qquad (14)$$

where P_s is the stationary intracavity pump power. As can be seen, ω_{max} decreases as the dispersion value $|\beta_2|$ increases. Thus the changing of the comb line spacing in Figure 8 coincides with the trend of the local dispersion curve in Figure 7F. More accurately, the analysis of modulational instability for the longitude modes ω_{-m} and ω_m involves their relative positions with respect to the pumped mode ω_0. Defining the resonance asymmetry factor $D_m = \omega_m - \omega_0 - (\omega_0 - \omega_{-m})$, the equivalent dispersion for modes ω_{-m} and ω_m is then

$$\beta_{2,eff} = -\frac{n_0 D_m}{cD_1^2 m^2} \qquad (15)$$

The analysis of modulational instability in section 3.1 is also applicable here as long as we replace the waveguide dispersion β_2 with the effective value $\beta_{2,eff}$ altered by mode coupling. It is worth noting that just one resonance shifting due to mode coupling, either the pumped mode or one of the two sideband modes, can be enough to achieve an equivalent anomalous dispersion (i.e. $\beta_{2,eff} < 0$, $D_m > 0$) and thus cause modulational instability for the two sideband modes.

In numerical simulations of the LL equation, the effect of mode coupling can be approximated simply by applying an additional phase shift to the comb sideband in the frequency domain of the split-step Fourier procedure. The modified LL equation is as follows

$$t_R \frac{\partial E(t,\tau)}{\partial t} = \left[-\alpha - i\delta_0 - iL\frac{\beta_2}{2}\frac{\partial^2}{\partial\tau^2} + i\gamma L|E|^2 + i[\Delta\phi]\right]E$$
$$+ \sqrt{\theta}E_{in} \qquad (16)$$

where the term $i[\Delta\phi]E$ means a phase shift of $\Delta\phi$ is applied only to the frequency components of E that have
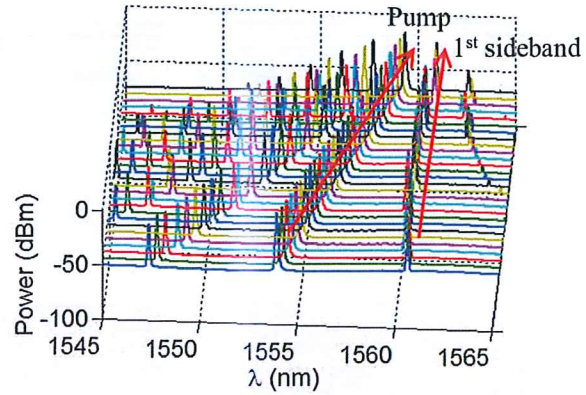

Figure 8: Experimental comb spectra generated due to mode coupling induced modulational instability. The pump laser pumps different resonances of mode 1 in the region marked with a green box in Figure 7C. One comb sideband is always pinned at a position close to the mode-crossing wavelength. Adapted from Ref. [45].

coupling with other transverse modes. The phase shift per round trip can be estimated by $\Delta\phi = -2\pi\Delta f/\text{FSR}$ where Δf is the mode coupling induced resonance shift. Figure 9 shows one simulation example. The initial intracavity field is the stationary cw solution on the upper branch plus weak noise. With the additional phase shift applied to the 1st, 2nd and 3rd sideband, respectively, the amplitude of the corresponding modes ($\pm1^{st}$, $\pm2^{nd}$, $\pm3^{rd}$ modes) grows exponentially. Cascaded four-wave mixing sidebands are generated subsequently, resulting in stable frequency combs spaced by 1, 2 and 3 FSRs, respectively. The comb spectra have nonsymmetric shapes that are similar to the experimental observations in Figure 8. Similar simulation pictures were also reported in [40]. The comb power decreases rapidly with increasing wavelength from the pump, resulting in relatively narrow spectra. The temporal waveforms of the combs shown in Figure 8 will be discussed in the next section (see Figure 14).

Note that the energy loss due to coupling with other modes is neglected in Eq. (16). In Figure 7B, we can see a wavelength dependence of the transmission spectrum, which is due to changes in the Q factor change induced by mode coupling. A variation of the resonance extinction ratio can also be observed in the zoom-in spectrum in Figure 7E. Such effects are not included in the approximate treatment of Eq. (16). For more accurate modeling of comb generation in the presence of mode coupling, it may be useful to investigate coupled LL equations with the nonlinearity, loss and dispersion of both modes considered. Such an analysis will be more complex than that based on Eq. (16) and has not yet been reported.
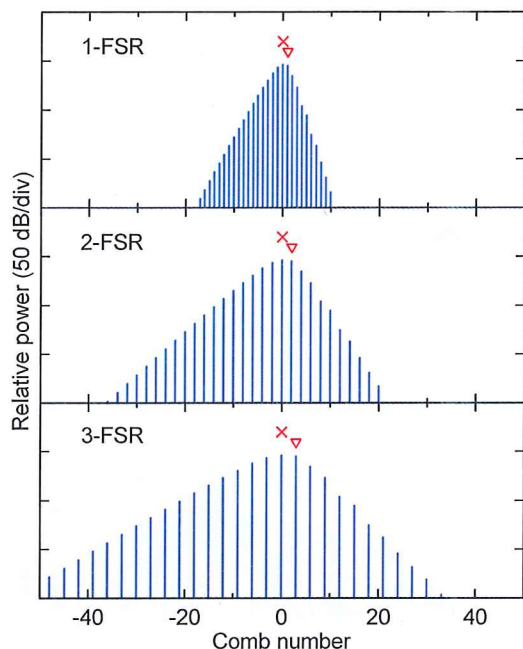
Figure 9: Simulated comb spectra based on normalized LL equation modified to take into account the mode coupling. The resonance shift induced by mode coupling is represented by an additional phase shift to the corresponding frequency component in the frequency domain of the split-step Fourier procedure. By applying an additional phase shift to the sidebands (marked with "▽") 1-, 2-, and 3-FSR away from the pump (marked with "×"), combs spaced by 1, 2, and 3 FSRs are generated, respectively. The simulation parameters are $\eta = 1$, $\Delta = 2.45$, $S = 3.45$, $\Delta\phi = -5.31$, FSR = 0.0054. LL: Lugiato–Lefever; FSR: free spectral range.

As discussed in the next section, when the pump is tuned into the resonance, the combs generated initially under modulational instability may transition into new states, potentially with substantially broader spectra. We have found that the simple model of Eq. (16) is sufficient to reproduce the experimental observations, provided that changes in the resonance shifts induced by the mode coupling (arising, for example, due to different thermal shifts for the associated modes) are included.

4 Mode-locking and time-domain characterization

Coherence and mode-locking properties are important metrics for the performance of frequency combs. In mode-locked states, the comb lines have stable amplitude and relative phase, giving rise to a stable time-domain waveform that does not change with time. Mode-locked states correspond to stable solutions of LL equation. In exper-

iments, the mode-locking properties can be investigated through time-domain characterization.

4.1 Type-I and-II combs and spectral line-by-line shaping

The first time-domain characterization of Kerr combs was performed through spectral line-by-line shaping of frequency combs generated in normal dispersion Si_3N_4 microrings [31]. The experimental scheme is shown in Figure 10. A pulse shaper based on a spatial light modulator [80] is used to tailor the amplitude and phase of each comb line after the microring. The waveform after shaping is diagnosed by measuring the second-order intensity autocorrelation [60]. In the line-by-line shaping procedure, the comb lines are selected one by one to pass through the pulse shaper. The phase shift applied to each comb line is optimized to maximize the second-harmonic strength at zero time delay. In this way, if the comb lines from the microring maintain a time-invariant relative phase profile (i.e., high coherence), their phases will be compensated to a uniform state after the pulse shaper, forming transform-limited pulses in the time domain. In contrast, transform-limited pulses cannot be obtained for low-coherence combs. A similar scheme was also employed in [32] to characterize the time-domain behavior of frequency combs from a fused quartz microresonator.
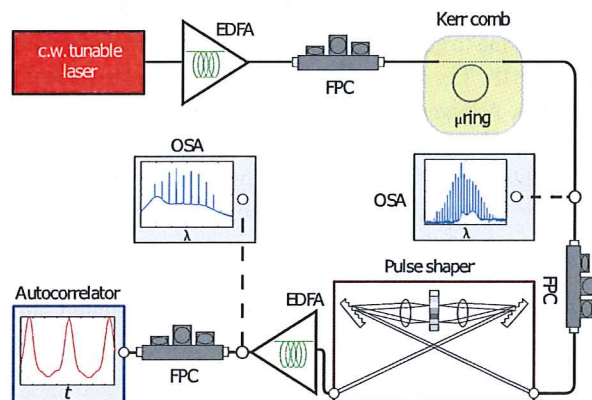

Figure 10: Experimental setup for spectral line-by-line shaping of microresonator Kerr frequency combs. EDFA: erbium-doped fiber amplifier; FPC: fiber polarization controller; μring: microring resonator; OSA: optical spectrum analyzer. Adapted by permission from Macmillan Publishers Ltd: Nature Photonics [31], copyright 2011.

We may distinguish two distinct paths to comb formation that exhibit different time-domain behaviors; these

are termed as type-I and -II combs in Ref. [31]. Type-I combs are generated as a cascade of sidebands spaced by a single FSR that spread from the pump. The cascade process replicates the frequency spacing of the initial sidebands, leading to a set of comb lines with precisely equal spacing. Type-II combs are generated first as sidebands spaced by multiple FSRs, after which more lines fill in to form combs with a single FSR spacing. The typical spectra of type-I and -II combs are shown in Figures 11A and 11B, respectively. Line-by-line pulse shaping experiments show that type-I combs can be shaped to closely transform-limited pulses, which reveals high coherence for this kind of combs. Figure 12A shows the spectrum before the intensity autocorrelator for the comb in Figure 11A. Also shown are the phase shifts applied to each comb line to maximize the second-harmonic strength at zero time delay. The measured autocorrelation trace after pulse shaping is shown in Figure 12B. For comparison, the trace measured without comb phase compensation (i.e., the phase transfer function of the pulse shaper is set to zero) and the trace calculated by assuming a uniform phase distribution across the comb spectrum are also shown. As can be seen, the autocorrelation trace without phase compensation shows very slight modulation while the trace after phase compensation gets a high extinction ratio that is very close to the result for transform-limited pulses. This provides clear evidence that the phases of the comb lines are locked, corresponding to high coherence. In comparison, type-II combs show a degraded compressibility. Figure 12C shows the spectrum before the autocorrelator and the phase applied to each line to generate compressed pulses for the comb in Figure 11B. The autocorrelation results are shown in Figure 12D. A large deviation is observed between the measured autocorrelation after phase compensation and the calculated result for ideal transform-limited pulses, suggesting substantially reduced coherence for type-II combs.

It is known that the contrast in intensity autocorrelation is a key feature that distinguishes isolated short pulses from continuous broadband noise [60]. The extinction ratio is ideally infinite for background-free short pulses, while limited to 2 for continuous broadband noise. Figure 13 shows the measured autocorrelation traces for a highly coherent comb and an incoherent comb that have broader spectra than those in Figure 12. The highly coherent comb can be clearly compressed; the autocorrelation background gets very close to zero after line-by-line phase compensation. In comparison, the extinction ratio for the incoherent comb is close to 2 and no improvement can be observed after line-by-line phase compensation. The comb
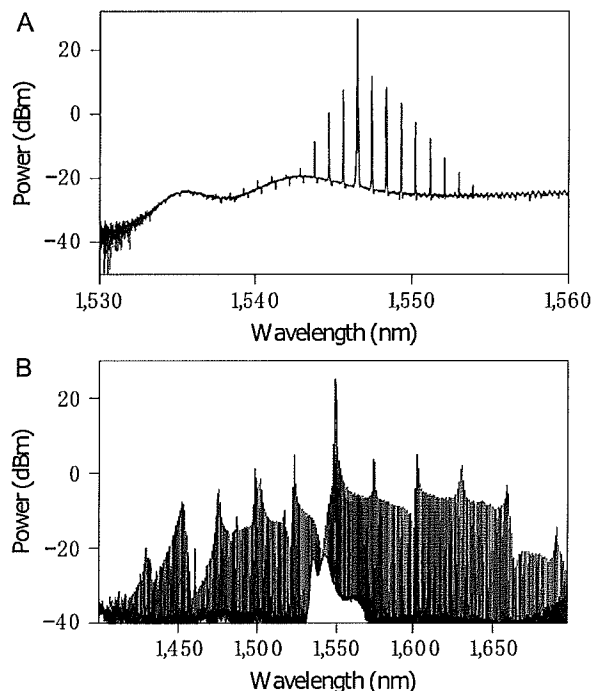

Figure 11: (A) Type-I and (B) type-II combs generated from a silicon nitride microring with radius 200 μm. The comb line spacing is ~115 GHz. Adapted by permission from Macmillan Publishers Ltd: Nature Photonics [31], copyright 2011.

phase randomly changes with time, corresponding to a randomly changing time domain waveform.

Note that the dispersion of the fiber link between the microring and the autocorrelator is not compensated in the experiments reported in Ref. [31], thus the intracavity waveform cannot be determined from the results of line-by-line shaping. In another measurement performed with a dispersion-compensated link, the autocorrelation is measured for a type-I comb from the drop port of a microring [42, 45]. It is found that the intracavity waveform of a type-I comb is close to transform-limited pulse (see Figure 14). Type-I combs in the normal dispersion regime are generated due to mode coupling induced modulational instability. This operating region is very similar to the so-called Turing-roll states in the anomalous dispersion regime [43, 54]. Figures 14C and 14D show the simulated comb spectrum and intracavity waveform using the method mentioned in Section 3.2 and estimated experimental parameters. Results close to the experimental observations are obtained.

The initial multi-FSR spaced comb lines in the formation of type-II combs in normal dispersion microresonators are generated due to mode coupling induced modulational instability. The generation of fill-in lines involves
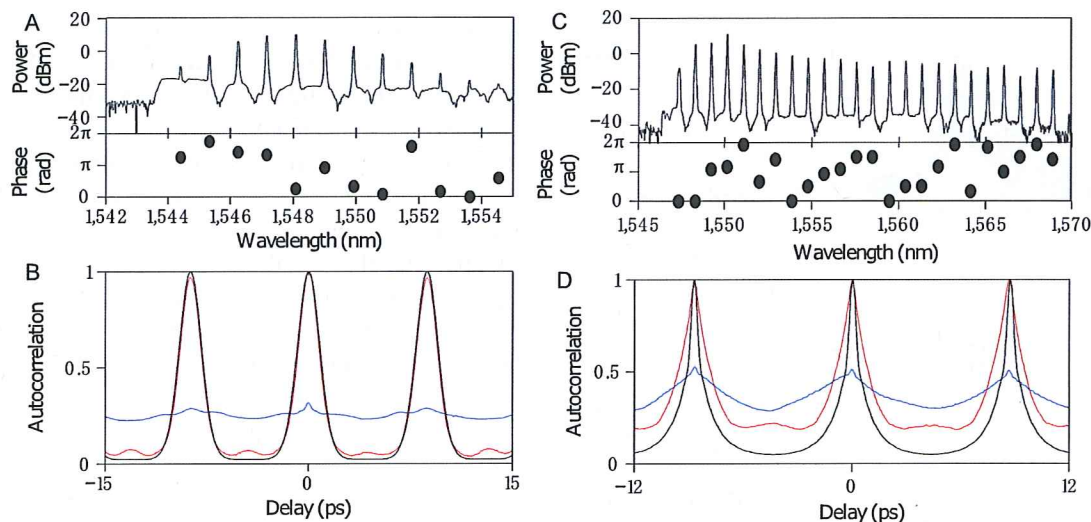
Figure 12: Different compressibility for (A, B) type-I and (C, D) type-II combs. (A), (C) Comb spectra before autocorrelator and phase shifts applied to each comb line by the pulse shaper. (B), (D) Intensity autocorrelation traces. Red: measured after phase compensation; black: calculated by assuming a flat comb spectral phase; blue: measured without phase compensation. Adapted by permission from Macmillan Publishers Ltd: Nature Photonics [31], copyright 2011.
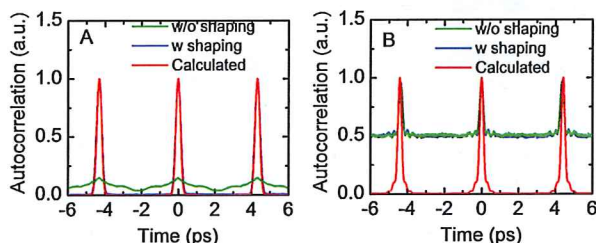

Figure 13: Autocorrelation traces for broadband (A) highly coherent comb and (B) incoherent comb. The comb line spacing is ~231 GHz. Measured results with (blue) and without (green) line-by-line shaping are shown. For the calculated results (red), a flat comb spectral phase is assumed. The data for panel B are provided by Pei-Hsun Wang in a private communication.

multiple degenerate or non-degenerate four-wave-mixing processes driven by the pump and the initial comb lines. Because of the microresonator dispersion, the cold-cavity resonances are not precisely evenly spaced. Thus there is nothing that guarantees exact subdivision of the frequency spacing when the lines fill in. Similar behavior can also be observed in anomalous dispersion combs, in which the initial and the fill-in lines are named primary and secondary combs in Ref. [33]. It is found that the fill-in lines may be composed of subcombs that have different offset frequencies, which is a possible explanation for the degraded compressibility of type-II combs reported in Ref. [31]. What appears to be one single comb line when displayed on a common low-resolution optical spectrum analyzer may in fact consist of multiple fine spectral struc-

tures that can be revealed by beating the comb line with a narrow-linewidth reference laser. Low frequency intensity noise in the MHz–GHz range corresponding to the beat notes between the subcombs can be detected by sending the comb to a photodetector. In experiments, detecting the comb intensity noise is a convenient way to monitor the comb dynamics and can provide preliminary information about the comb coherence [33, 35, 36, 41].

4.2 Dark pulse mode-locking transitions

It has been shown in the anomalous dispersion regime that under some conditions, initially noisy, Type II combs can undergo mode-locking transitions resulting in generation of one or more stable cavity solitons circulating within the microresonator [36]. Such cavity solitons resemble the bright soliton pulses from anomalous dispersion nonlinear fiber optics but sitting on a finite background. Our group has shown that mode-locking transitions can also occur in normal dispersion microresonators, resulting in formation of mode-locked dark pulses [46]. Such dark pulses are localized structures balanced by dispersion, Kerr nonlinearity, parametric gain, and cavity loss. It was demonstrated that dark pulses can be excited by mode coupling induced modulational instability. Dark pulses may be formed when the combs transition from high-noise, low-coherence states to low-noise, high-coherence states. Compared to modulational instability sidebands
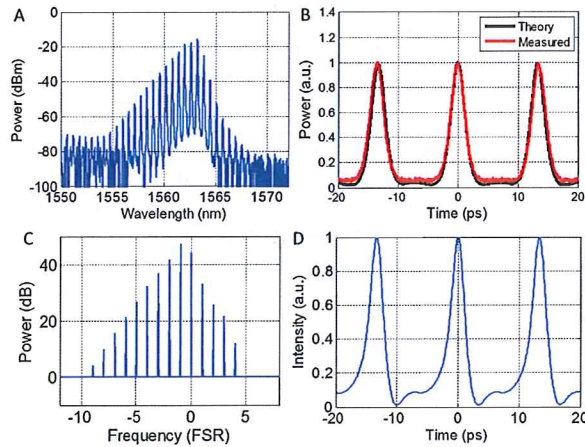
Figure 14: Intracavity waveform of type-I comb. (A) Spectrum of a type-I comb measured at the drop port of a Si_3N_4 microring. The comb line spacing is ~75 GHz. (B) Autocorrelation trace measured with a dispersion-compensated link and no spectral phase compensation. For the calculated result, a flat comb spectral phase is assumed. (C), (D) Simulated comb spectrum and waveform based on estimated experimental parameters. Adapted from Ref. [45]. FSR: free spectral range.

in Figure 14, dark pulse combs have much broader spectra. Transitions from modulation instability sidebands to dark pulses may occur when the pump laser detuning is changed. It is interesting to note that mode coupling induced modulational instability is required to excite the dark pulses but is not necessary to maintain them. Dark pulses are stable structures that can exist in normal dispersion cavities without any mode crossings, where the cavity loss for each comb line is balanced by gain from its mixing with the pump and other comb lines.

It has been observed in both simulations and experiments that prior to formation of stable bright solitons in anomalous dispersion cavities, the comb passes through a chaotic state. Therefore, the mode-locked solitons have a stochastic excitation pathway, meaning that different number of soliton peaks may be generated for each experimental trial [36, 52, 56]. In comparison, the dark pulse mode-locking transitions reported in [46] show a rather deterministic pathway. Figure 15 shows the results of comb generation using a Si_3N_4 microring with a drop port. Two different resonances that are close to a mode-crossing position are pumped separately for Figures 15A-C and 15D-F. The power transmission measured at the drop port as the laser is tuned into resonance is shown in Figures 15A and 15D. Power drop steps related to transitions of the comb states can be observed. The measurements were repeated twenty times and overlaid; the various traces were nearly identical, showing that the transition behavior has

high repeatability. The comb spectra and intensity noise at each stage are shown in Figures 15B-C and 15E-F. Low-noise combs spaced by 1 and 2 FSRs are generated at stage III in Figures 15B and 15E. The time domain waveforms are measured by self-referenced cross-correlation. Part of the comb power is compressed to transform-limited bright pulses through line-by-line shaping and then used as a sampling signal to test the original waveform by measuring their cross-correlation. The cross-correlation results are shown in Figure 16. For the 1-FSR comb, one dark pulse per roundtrip can be observed; while for the 2-FSR comb, two dark pulses can be observed.
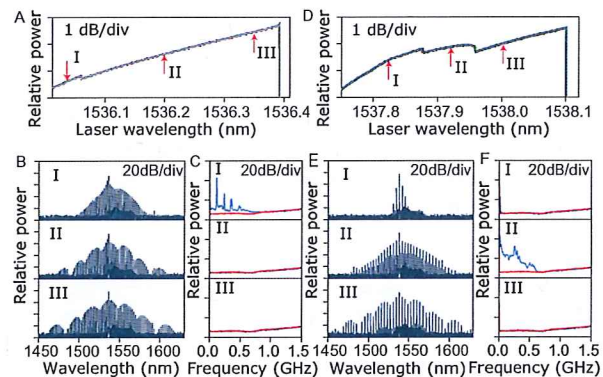

Figure 15: Low-noise, mode-locking transitions related to dark pulse formation. Two resonances close to mode-crossing position are pumped separately for A-C and D-F. (A), (D) Power transmission measured at the drop port. Twenty traces are overlaid with different colors. (B), (E) Comb spectra and (C), (F) intensity noise at different stages of comb development. The comb spacing is ~231 GHz. Adapted by permission from Macmillan Publishers Ltd: Nature Photonics [46], copyright 2015.

Different from single bright soliton combs, which usually have smooth spectra [36], the dark pulse combs tend to have spectral variations, as can be observed in Figure 15. Figure 17 shows another mode-locked dark pulse comb with a slightly different spectral envelope, generated from a different Si_3N_4 microring [46]. The time-domain waveform is reconstructed based on the spectral intensity and the phase profile retrieved through line-by-line shaping. Since only a through waveguide is available for this microring, the field at the through port is the superposition of the comb line from the cavity on top of the strong co-propagating pump. To reconstruct the waveform inside the cavity; the amplitude and phase of the pump line measured at the through port needs to be corrected by considering the bus-microresonator coupling condition and the nonlinear loss of the pump related to comb generation (see supplementary material of [46] for the detailed proce-
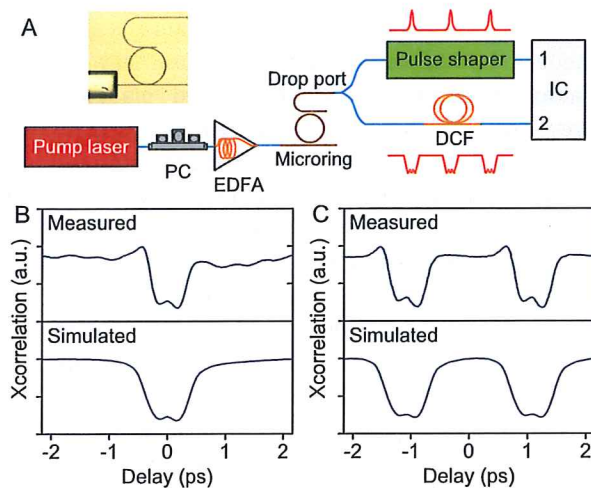
Figure 16: Time-domain characterization of dark pulse combs through spectral line-by-line shaping and self-referenced cross-correlation. (A) Experimental setup. The inset shows a microscope image of the Si_3N_4 microring with both a through port (lower) and a drop port (upper). (B), (C) Cross-correlation results for the combs in Figures 15B III and 15E III, respectively. PC: polarization controller; EDFA: erbium-doped fiber amplifier; DCF: dispersion compensating fiber; IC: intensity correlator. Adapted by permission from Macmillan Publishers Ltd: Nature Photonics [46], copyright 2015.

Figure 17: Complex chirp structure of dark pulses. (A) Comb spectrum and phase. The phase profile marked in red is retrieved through line-by-line shaping. The green part is out of the pulse shaper's passband and is estimated based on spectral symmetry. The comb is tested at the through port and is thus superimposed on the pump field from the input waveguide. The intracavity pump amplitude and phase are estimated based on the cavity coupling condition and the nonlinear loss induced by comb generation. (B) Reconstructed intracavity waveform. Inst. freq.: instantaneous frequency. Adapted by permission from Macmillan Publishers Ltd: Nature Photonics [46], copyright 2015.

dure). Complex frequency chirp structures can be clearly observed in Figure 17B. Note that such dark pulses in microresonators differ from the topological dark solitons found in normal dispersion single-mode fibers [81, 82]. The fiber dark solitons have a π-phase shift between the background levels, which is incompatible with the periodic boundary conditions imposed in a cavity. Simulations show that the formation of dark pulses is related to interactions of switching waves in the microresonator. Switching waves are wave fronts connecting the two stable stationary cw solutions in the cavity, which were previously studied in the context of spatial dynamics in nonlinear cavities [83] and were also observed in the temporal domain in fiber cavities [84]. When two switching waves get close, they may be trapped by each other, as a result generating stable dark pulses. Depending on the pump power, detuning, and the excitation field, dark pulses with different spectral and time-domain features may be generated. Figure 18 shows some simulation results of dark pulse formation from switching waves. The initial fields contain two well-separated steps corresponding to two switching waves. The constant field values connected by the steps correspond to the stable cw solutions of the nonlinear cavity in both amplitude and phase. The two switching waves then move towards each other and finally stop to generate a stable dark pulse.
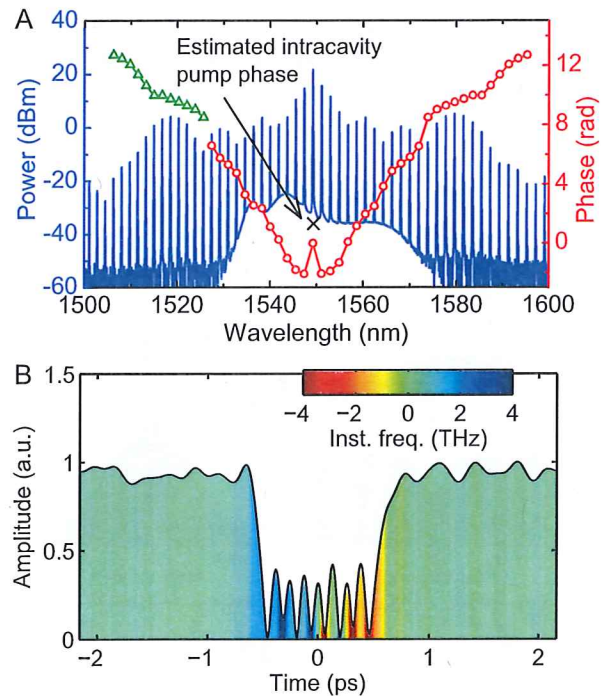
The initial comb lines generated by mode coupling induced modulational instability provide a weak perturbation which stimulates switching waves and dark pulses. As the pump laser is tuned into the resonance from the blue side, the modulational instability gain may change due to several reasons. First, the laser-resonance detuning changes; second, the different transverse modes have different thermal shifting rates and thus the relative positions of the coupled resonances change; third, the mode coupling coefficient may have a wavelength dependence (see Figure 7). The comb state transitions are usually accompanied by such change in the mode coupling induced resonant shifts. In the case when modulational instability gain decreases with the increase of detuning, the switching waves and dark pulses tend to have a flat upper-branch background. However, in Figures 16B and 16C, the impact of mode coupling can still be observed from the background variations of the measured dark pulse profiles. In

some cases, the dark pulse becomes strongly distorted due to the presence of mode coupling (see Figure S6 in Supplementary of Ref. [46]).
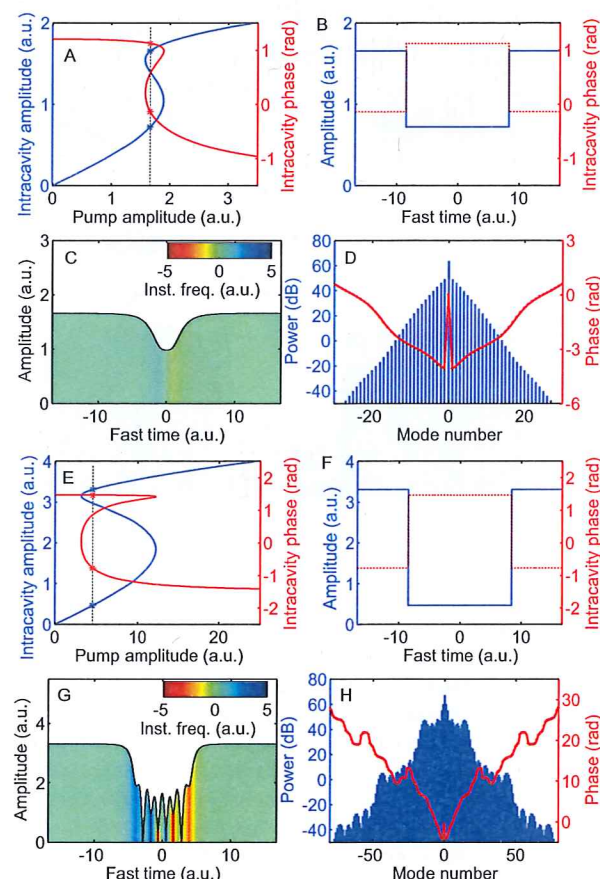

Figure 18: Dark pulse formation from two well-separated switching waves. (A, E) Bistability curve. (B, F) Initial waveform. (C, G) Dark pulse evolved from the initial waveform. Inst. freq.: instantaneous frequency. (D, H) Corresponding comb spectra. The simulations are based on normalized LL equation with $\eta = 1$. The normalized round-trip time $t'_R = 33.33$. The initial spacing between the two switching waves is $t'_R/2$. For (A)-(D), $\Delta = 2.61$, $S = 1.67$; for (E)-(H), $\Delta = 10$, $S = 4.57$. Since the general LL equation uses an $\exp(-i\omega t)$ convention [58], while the experiments use the $\exp(i\omega t)$ convention common in ultrafast optics [60] (see Figure 17A), the sign of the phase plotted in A, B, D, E, F, H is inverted compared with the actual simulation results.

4.3 Bright pulse generation

In some cases, the intracavity waveforms for normal dispersion microresonators may be affected by several factors and appear as short bright pulses rather than dark pulses. In Ref. [55], Lobanov et al. showed through numerical sim-

ulations that when the pumped resonance is shifted by mode coupling, the intracavity waveform may look like flat-top bright pulses, which they named "platicons". Figure 19 shows the simulated results. The width of the bright pulse can be controlled by changing the pump laser detuning. It is also pointed out that for periodic waveforms in the microresonators, the difference between bright and dark pulses diminishes. The platicons may be considered equivalently as low duty factor bright pulses or high duty factor dark pulses. The duty factor may change when the pump laser power, detuning or the mode coupling induced resonance shift is varied.

Huang et al. reported ultrashort pulse generation from a Si_3N_4 microring that is reported to have weak global normal dispersion [48]. Figure 20A shows the comb spectrum. Figure 20B shows the time-domain waveform measured using frequency-resolved optical gating (FROG) method. A 74-fs bright pulse is observed. It is reported that the wavelength dependent loss inside the microring plays a role in determining the pulse shape. Figure 20C shows the loaded Q factors measured in a wide wavelength range. The Q roll-off at long wavelengths is due to the increase of coupling loss, while at the short wavelength, it is due to absorption from the residual N-H bounds. It should be noted that the ultrashort pulse in [48] is measured at the through port outside the microring. As discussed briefly in connection with Fig. 17 above and in detail in [46], the complex amplitude of the intracavity pump field may substantially differ from that measured at the through port output. Therefore, the relationship of the amplitude and phase of the pulse relative to the background field inside the cavity (this relationship governs whether a pulse is considered bright or dark) may also differ substantially from what is shown in Fig. 20, leaving the actual intracavity waveform unknown.
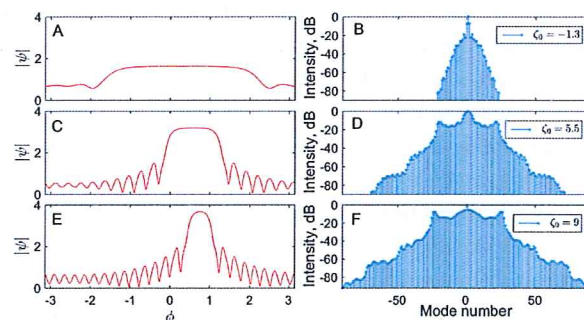

Figure 19: (A, C, E) Numerically simulated platicons in normal dispersion microresonators for different values of laser detuning. (B, D, F) Corresponding optical spectra for the same set of parameters. Adapted from Ref. [55]. Refer to [55] for the details of simulation parameters.
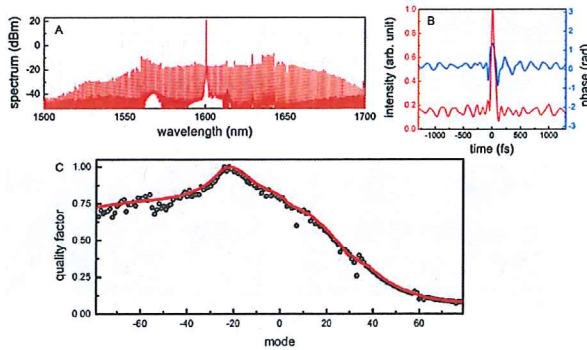
Figure 20: Bright pulse generation from a Si_3N_4 microring with wavelength-dependent Q factors. (A) Optical spectrum. The comb line spacing is ~115 GHz. (B) Time-domain waveform at microring through port measured with FROG. (C) Loaded Q factors (in million-scale). Larger mode numbers correspond to shorter wavelength. Adapted from Ref. [48].

5 Reliable comb generation and control

High reliability and controllability are required for practical applications. Some techniques developed for this purpose in the normal dispersion regime are described below.

5.1 Microheater-actuated comb generation and spectrum tuning

A microheater actuated comb generation scheme is proposed in Ref. [46]. The device picture is shown in Figure 21A. A microheater is integrated on top of a Si_3N_4 microring resonator. By changing the voltage applied on the heater, the microresonator resonance can be shifted due to thermal expansion and the thermo-optic effect. Thermal tuning provides one more degree of control for comb generation, supplementing the traditional methods of changing the pump laser power and wavelength. With thermal tuning, one can generate frequency combs with a wavelength-fixed laser; this may reduce the system complexity for some applications. Figure 21B illustrates the details of this method. The resonance needs to be first tuned to the red side of the pump laser, and then tuned back towards the blue. Physically it is equivalent to the traditional method of tuning the laser wavelength from blue to red into the resonance. Frequency combs have been generated in this way in Ref. [46]; low-noise mode-locking transitions related to dark pulse formation are observed.

After the mode-locked comb is obtained, it can be further tuned by tuning the pump laser and the resonator in tandem. Figure 21C shows the comb spectra when the comb center wavelength is tuned by 75%×FSR (~1.4 nm). The comb envelope remains substantially unchanged in the process. Transform-limited pulses could always be obtained through spectral line-by-line shaping after spectral tuning (see Figure 21D), suggesting that the coherent mode-locked state is maintained. It is worth noting that since the mode-locked comb state is sensitive to the pump-resonance detuning, it is required that the detuning remain substantially the same in order to maintain a coherent comb state. As a result, the use of a microheater was instrumental to achieving such wideband tuning. Spectral tuning of Kerr combs is potentially important for many applications, such as aligning the comb wavelengths to the channels in wavelength-division multiplexed communications.
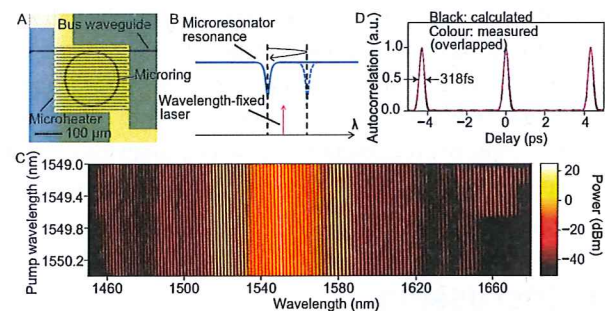

Figure 21: Microheater-actuated comb generation and tuning. (A) Microscope image of a Si_3N_4 microring integrated with a microheater. The ring radius is 100 μm. (B) Illustration of comb generation by tuning the resonance. (C) Comb spectra with the center wavelength tuned from 1549.0 to 1550.4 nm with an increment of 0.1 nm. The comb line spacing is ~231 GHz. (D) Autocorrelation traces for each comb in (C) after spectral line-by-line shaping. All the combs can be compressed to transform-limited pulses, suggesting high coherence. Adapted by permission from Macmillan Publishers Ltd: Nature Photonics [46], copyright 2015.

5.2 Programmable mode coupling control with dual-coupled microresonators

The mode coupling between different transverse modes or polarization modes in a single microresonator relies on accidental degeneracy of the modes and is therefore very difficult to control. A dual-coupled microresonator scheme was proposed in Ref. [47] to introduce programmable mode coupling for reliable comb generation in the normal

dispersion regime. Similar structures have been demonstrated previously for high-efficiency on-chip four-wave mixing [85]. Figure 22A shows the microscope image of the Si_3N_4 rings reported in Ref. [47], consisting of one main and one auxiliary ring. Accidental mode degeneracies are avoided by tailoring waveguide cross-section to achieve single transverse mode per polarization. The measured dispersion of the ring waveguide is $\beta_2 \approx 130\,ps^2/km$ (normal dispersion regime). The two rings have slightly different FSRs as shown in Figure 22B. Mode coupling now takes place between the two rings. The mode crossing wavelength can be controlled by tuning the auxiliary ring with a microheater. Figure 22C shows the transmission spectroscopy of the main ring. As can be seen, the resonances of the main ring can be selectively split and shifted. In comb generation, the laser pumps the main ring while the auxiliary ring is thermally tuned to control the mode splitting. Comb generation is demonstrated and shows high controllability. By selecting the mode splitting wavelength, the comb repetition rate can be selected. Figure 22D shows the comb spectra when the comb line spacing is changed from 1 FSR to 6 FSRs. Low-noise, mode-locking transitions are also observed. Figure 22E shows one example of broadband mode-locked comb that can be compressed to transform-limited ultrashort pulses.

6 Discussion

Normal-dispersion microcombs are now attracting increasing attention in the research community. It is shown in Ref. [55] through numerical simulations that one potential advantage of normal-dispersion microcombs compared with anomalous-dispersion ones is that they may achieve a higher power conversion efficiency. The higher conversion efficiency may be advantageous for some applications such as comb-based photonic RF signal processing [7] and fiber communications—and, in general, for any application that is sensitive to power efficiency.

One potential application of microcombs is optical frequency synthesis based on self-referencing for which ultra-wideband combs spanning close to one octave are required. The dispersion is one factor limiting the comb bandwidth. In the anomalous dispersion regime, mode-locked microcombs spanning up to 2/3 of an octave have been demonstrated by tailoring the dispersion close to zero [86]. In comparison, the coherent normal dispersion microcombs demonstrated so far are well below one octave. In the future, it will be interesting to explore the potential of generating ultra-wideband microcombs with
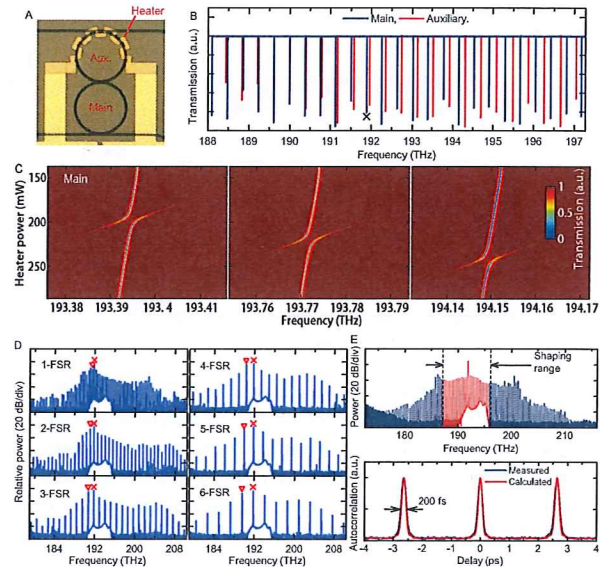

Figure 22: Reliable comb generation with dual-coupled microresonators. (A) Microscope image of dual-coupled Si_3N_4 microrings. The radii of the main and auxiliary rings are 60 and 58 μm, respectively. The cross-section dimension of the ring waveguide is 1.3 μm×600 nm. The coupling gap between the two rings is 600 nm. (B) Transmission of the two rings measured at their respective bus waveguide. The FSRs of the main and auxiliary rings are 378 GHz and 391 GHz, respectively. (C) Transmission spectroscopy of the main ring when the mode splitting is tuned by thermally tuning the auxiliary ring. (D) Repetition rate selectable comb generation. The comb line marked with "×" is the pump line; the comb line marked with "∇" is where mode crossing happens. (E) Upper: spectrum of a broadband mode-locked comb after transition to a low-noise state; lower: autocorrelation of the compressed pulse after line-by-line phase compensation. Adapted from Ref. [47].

very low normal dispersion. As in the anomalous dispersion regime [86], it may also prove important to tailor higher order dispersion terms to further increase the comb bandwidth. The impact of higher order dispersion as well as other effects such as Raman scattering needs to be further investigated. Moreover, it will be important to investigate the generation of normal-dispersion microcombs in the visible and near infrared range where material dispersion dominates. New candidates of nonlinear materials and microresonator designs may become possible in the normal dispersion regime.

References

[1] Ye J, Cundiff ST. Femtosecond Optical Frequency Comb: Principle, Operation, and Applications. Boston, MA, USA, Springer, 2005.

[2] Udem Th, Holzwarth R, Hänsch TW. Optical frequency metrology. Nature 2002; 416: 233–237.

[3] Ye J, Schnatz H, Hollberg LW. Optical frequency combs: from frequency metrology to optical phase control. J Sel Top Quantum Electron 2003; 9: 1041–1058.

[4] Adler F, Thorpe MJ, Cossel KC, Ye J. Cavity-enhanced direct frequency comb spectroscopy: technology and applications. Annu. Rev. Anal. Chem. 2010; 3: 175–205.

[5] Fortier TM, Kirchner MS, Quinlan F, et al. Generation of ultrastable microwaves via optical frequency division. Nature Photon 2011; 5: 425–429.

[6] Supradeepa VR, Long CM, Wu R. Comb-based radiofrequency photonic filters with rapid tunability and high selectivity. Nature Photon 2012; 6: 186–194.

[7] Xue X, Xuan Y, Kim HJ, et al. Programmable single-bandpass photonic RF filter based on Kerr comb from a microring. J Lightwave Technol 2014; 32: 3557–3565.

[8] Liang W, Eliyahu D, Ilchenko VS, et al. High spectral purity Kerr frequency comb radio frequency photonic oscillator. Nature Commum 2015; 6: 7957.

[9] Hillerkuss D, Schmogrow R, Schellinger T, et al. 26 Tbit s^{-1} line-rate super-channel transmission utilizing all-optical fast Fourier transform processing. Nature Photon 2011; 5: 364–371.

[10] Hillerkuss D, Schmogrow R, Meyer M, et al. Single-laser 32.5 Tbit/s Nyquist WDM transmission. J Opt Commun Netw 2012; 4: 715–723.

[11] Pfeifle J, Brasch V, Lauermann M, et al. Coherent terabit communications with microresonator Kerr frequency combs. Nature Photon 2014; 8: 375–380.

[12] Fermann ME, Hartl I. Ultrafast fibre lasers. Nature Photon 2013; 7: 868–874.

[13] Torres-Company V, Weiner AM. Optical frequency comb technology for ultra-broadband radio-frequency photonics. Laser Photon Rev 2014; 8: 368–393.

[14] Kippenberg TJ, Holzwarth R, Diddams SA. Microresonator-based optical frequency combs. Science 2011; 332: 555–559.

[15] Kippenberg TJ, Spillane SM, Vahala KJ. Kerr-nonlinearity optical parametric oscillation in an ultrahigh-Q toroid microcavity. Phys Rev Lett 2004; 93: 083904.

[16] Savchenkov AA, Matsko AB, Strekalov D, Mohageg M, Ilchenko VS, Maleki L. Low threshold optical oscillations in a whispering gallery mode CaF2 resonator. Phys Rev Lett 2004; 93: 243905.

[17] Del'Haye P, Schliesser A, Arcizet O, Wilken T, Holzwarth R, Kippenberg TJ. Optical frequency comb generation from a monolithic microresonator. Nature 2007; 450: 1214–1217.

[18] Agha IH, Okawachi Y, Foster MA, Sharping JE, Gaeta AL. Four-wave-mixing parametric oscillations in dispersion-compensated high-Q silica microspheres. Phys Rev A 2007; 76: 043837.

[19] Papp SB, Del'Haye P, Diddams SA. Mechanical control of a microrod-resonator optical frequency comb. Phys Rev X 2013; 3: 031003.

[20] Savchenkov AA, Matsko AB, Ilchenko VS, Solomatine I, Seidel D, Maleki L. Tunable optical frequency comb with a crystalline whispering gallery mode resonator. Phys Rev Lett 2008; 101: 093902.

[21] Grudinin IS, Baumgartel L, Yu N. Frequency comb from a microresonator with engineered spectrum. Opt Express 2012; 20: 6604–6609.

[22] Wang CY, Herr T, Del'Haye P, et al. Mid-infrared optical frequency combs at 2.5 μm based on crystalline microresonators. Nature Commun 2013; 4: 1345.

[23] Ilchenko VS, Savchenkov AA, Matsko AB, Maleki L. Generation of Kerr frequency combs in a sapphire whispering gallery mode microresonator. Opt Eng 2014; 53: 122607.

[24] Razzari L, Duchesne D, Ferrera M, et al. CMOS-compatible integrated optical hyperparametric oscillator. Nature Photon 2009; 4: 41–45.

[25] Levy JS, Gondarenko A, Foster MA, Turner-Foster AC, Gaeta AL, Lipson M. CMOS-compatible multiple-wavelength oscillator for on-chip optical interconnects. Nature Photon 2009; 4: 37–40.

[26] Jung H, Xiong C, Fong KY, Zhang X, Tang HX. Optical frequency comb generation from aluminum nitride microring resonator. Opt Lett 2013; 38: 2810–2813.

[27] Hausmann BJM, Bulu I, Venkataraman V, Deotare P, Lončar M. Diamond nonlinear photonics. Nature Photon 2014; 8: 369–375.

[28] Griffith AG, Lau RKW, Cardenas J, et al. Silicon-chip mid-infrared frequency comb generation. Nature Commun 2015; 6: 6299.

[29] Del'Haye P, Herr T, Gavartin E, Gorodetsky ML, Holzwarth R, Kippenberg TJ. Octave spanning tunable frequency comb from a microresonator. Phys Rev Lett 2011; 107: 063901.

[30] Okawachi Y, Saha K, Levy JS, Wen YH, Lipson M, Gaeta AL. Octave-spanning frequency comb generation in a silicon nitride chip. Opt Lett 2011; 36: 3398–3400.

[31] Ferdous F, Miao H, Leaird DE, et al. Spectral line-by-line pulse shaping of on-chip microresonator frequency combs. Nature Photon 2011; 5: 770–776.

[32] Papp SB, Diddams SA. Spectral and temporal characterization of a fused-quartz-microresonator optical frequency comb. Phys Rev A 2011; 84: 053833.

[33] Herr T, Hartinger K, Riemensberger J, et al. Universal formation dynamics and noise of Kerr-frequency combs in microresonators. Nature Photon 2012; 6: 480–487.

[34] Li J, Lee H, Chen T, Vahala KJ. Low-pump-power, low-phase-noise, and microwave to millimeter-wave repetition rate operation in microcombs. Phys Rev Lett 2012; 109: 233901.

[35] Saha K, Okawachi Y, Shim B, et al. Modelocking and femtosecond pulse generation in chip-based frequency combs. Opt Express 2013; 21: 1335–1343.

[36] Herr T, Brasch V, Jost JD, et al. Temporal solitons in optical microresonators. Nature Photon 2014; 8: 145–152.

[37] Del'Haye P, Beha K, Papp SB, Diddams SA. Self-injection locking and phase-locked states in microresonator-based optical frequency combs. Phys Rev Lett 2014; 112: 043905.

[38] Herr T, Brasch V, Jost JD, et al. Mode spectrum and temporal soliton formation in optical microresonators. Phys Rev Lett 2014; 113: 123901.

[39] Del'Haye P, Coillet A, Loh W, Beha K, Papp SB, Diddams SA. Phase steps and resonator detuning measurements in microresonator frequency combs. Nature Commun 2015; 6: 5668.

[40] Savchenkov AA, Matsko AB, Liang W, Ilchenko VS, Seidel D, Maleki L. Kerr frequency comb generation in overmoded resonators. Opt Express 2012; 20: 27290–27298.

[41] Wang PH, Ferdous F, Miao H, et al. Observation of correlation between route to formation, coherence, noise, and communication performance of Kerr combs. Opt Express 2012; 20: 29284–29295.

[42] Wang PH, Xuan Y, Fan L, et al. Drop-port study of microresonator frequency combs: power transfer, spectra and time-domain characterization. Opt Express 2013; 21: 22441–22452.

[43] Coillet A, Balakireva I, Henriet R, et al. Azimuthal Turing patterns, bright and dark cavity solitons in Kerr combs generated with whispering-gallery-mode resonators. Photon J 2013; 5: 6100409.

[44] Liang W, Savchenkov AA, Ilchenko VS, et al. Generation of a coherent near-infrared Kerr frequency comb in a monolithic microresonator with normal GVD. Opt Lett 2014; 39: 2920–2923.

[45] Liu Y, Xuan Y, Xue X, et al. Investigation of mode coupling in normal-dispersion silicon nitride microresonators for Kerr frequency comb generation. Optica 2014; 1: 137–144.

[46] Xue X, Xuan Y, Liu Y, et al. Mode-locked dark pulse Kerr combs in normal-dispersion microresonators. Nature Photon 2015; 9: 594–600.

[47] Xue X, Xuan Y, Wang PH, et al. Normal-dispersion microcombs enabled by controllable mode interactions. Laser Photon Rev 2015; 9: 4, L23–L28.

[48] Huang SW, Zhou H, Yang J, et al. Mode-locked ultrashort pulse generation from on-chip normal dispersion microresonators. Phys Rev Lett 2015; 114: 053901.

[49] Matsko AB, Savchenkov AA, Liang W, Ilchenko VS, Seidel D, Maleki L. Mode-locked Kerr frequency combs. Opt Lett 2011; 36: 2845–2847.

[50] Matsko AB, Savchenkov AA, Maleki L. Normal group-velocity dispersion Kerr frequency comb. Opt Lett 2012; 37: 43–45.

[51] Coen S, Randle HG, Sylvestre T, Erkintalo M. Modeling of octave-spanning Kerr frequency combs using a generalized mean-field Lugiato–Lefever model. 2013; 38: 37–39.

[52] Lamont MRE, Okawachi Y, Gaeta AL. Route to stabilized ultra-broadband microresonator-based frequency combs. Opt Lett 2013; 38: 3478–3479.

[53] Parra-Rivas P, Gomila D, Matías MA, Coen S, Gelens L. Dynamics of localized and patterned structures in the Lugiato-Lefever equation determine the stability and shape of optical frequency combs. Phys Rev A 2014; 89: 043813.

[54] Godey C, Balakireva IV, Coillet A, Chembo YK. Stability analysis of the spatiotemporal Lugiato-Lefever model for Kerr optical frequency combs in the anomalous and normal dispersion regimes. Phys Rev A 2014; 89: 063814.

[55] Lobanov VE, Lihachev G, Kippenberg TJ, Gorodetsky ML. Frequency combs and platicons in optical microresonators with normal GVD. Opt Express 2015; 23: 7713–7721.

[56] Jaramillo-Villegas JA, Xue X, Wang PH, Leaird DE, and Weiner AM. Deterministic single soliton generation and compression in microring resonators avoiding the chaotic region. Opt Express 2015; 23: 9618-9626.

[57] Agrawal GP. Nonlinear Fiber Optics. San Diego, CA, USA, Academic Press, 2001.

[58] Haelterman M, Trillo S, Wabnitz S. Dissipative modulation instability in a nonlinear dispersive ring cavity. Opt Commun 1992; 91: 401–407.

[59] Coen S, Haelterman M. Modulational instability induced by cavity boundary conditions in a normally dispersive optical fiber. Phys Rev Lett 1997; 79: 4139–4142.

[60] Weiner AM. Ultrafast Optics. Hoboken, NJ, USA, John Wiley & Sons, 2009.

[61] Haus HA, Fujimoto JG, and Ippen EP. Structures for additive pulse mode locking. J Opt Soc Am 1991; 8: 2068–2076.

[62] Tamura K, Ippen EP, Haus HA, and Nelson LE. 77-fs pulse generation from a stretched-pulse mode-locked all-fiber ring laser. Opt Lett 1993; 18: 1080–1082.

[63] Chong A, Buckley J, Renninger W, and Wise F. All-normal-dispersion femtosecond fiber laser. Opt Exp 2006; 14: 10095–10100.

[64] Del'Haye P, Arcizet O, Gorodetsky ML, Holzwarth R, Kippenberg TJ. Frequency comb assisted diode laser spectroscopy for measurement of microcavity dispersion. Nature Photon 2009; 3: 529–533.

[65] Zhang L, Mu J, Singh V, Agarwal AM, Kimerling LC, Michel J. Intra-cavity dispersion of microresonators and its engineering for octave-spanning Kerr frequency comb generation. IEEE J Sel Top Quantum Electron 2014; 20: 5900207.

[66] Refractive Index Database and the references therein. (Accessed October 4, 2015, at http://refractiveindex.info).

[67] Grudinin IS, Yu N. Dispersion engineering of crystalline resonators via microstructuring. Optica 2015; 2: 221–224.

[68] Turner AC, Manolatou C, Schmidt BS, Lipson M. Tailored anomalous group-velocity dispersion in silicon channel waveguides. Opt Express 2006; 14: 4357–4362.

[69] Willner AE, Zhang L, Yue Y. Tailoring of dispersion and nonlinear properties of integrated silicon waveguides for signal processing applications. Semicond Sci Technol 2011; 26: 014044.

[70] Riemensberger J, Hartinger K, Herr T, Brasch V, Holzwarth R, Kippenberg TJ. Dispersion engineering of thick high-Q silicon nitride ring-resonators via atomic layer deposition. Opt Express 2012; 20: 27661–27669.

[71] Chavez Boggio JM, Bodenmüller D, Fremberg T, et al. Dispersion engineered silicon nitride waveguides by geometrical and refractive-index optimization. J Opt Soc Am B 2014; 31: 2846–2857.

[72] Coen S, Haelterman M, Emplit P, Delage L, Simohamed LM, Reynaud F. Bistable switching induced by modulational instability in a normally dispersive all-fibre ring cavity. J Opt B 1999; 1: 36–42.

[73] Carmon T, Yang L, Vahala KJ. Dynamical thermal behavior and thermal self-stability of microcavities. Opt Express 2004; 12: 4742–4750.

[74] Ghosh G. Handbook of Optical Constants of Solids: Handbook of Thermo-Optic Coefficients of Optical Materials with Applications. 1st ed. Academic Press, 1998.

[75] Berkhoer AL, Zakharov VE. Self excitation of waves with different polarizations in nonlinear media. Zh Eksp Teor Fiz 1970; 58: 903–911 [J Exp Theor Phys 1970; 31: 486–490].

[76] Agrawal GP. Modulation instability induced by cross-phase modulation. Phys Rev Lett 1987; 59: 880–883.

[77] Zolotovskii IO, Petrov AN, Sementsov DI. Modulation instability of wave packets in the presence of linear and nonlinear mode coupling. Zh Eksp Teor Fiz 2006; 76: 90–95 [Tech Phys 2006; 51: 236–241].

[78] Haus HA, Popović MA, Watts MR, Manolatou C, Little BE, Chu ST. Optical resonators and filters. In: Vahala K, ed. Optical Mi-

crocavities. Singapore, World Scientific Publishing, 2004, 9.

[79] Grudinin IS, Baumgartel L, and Yu N. Impact of cavity spectrum on span in microresonator frequency combs. Opt Exp 2013; 21: 26929–26935.

[80] Weiner AM. Femtosecond pulse shaping using spatial light modulators. Rev Sci Instrum 2000; 71: 1929–1960.

[81] Weiner AM, Heritage JP, Hawkins RJ, et al. Experimental observation of the fundamental dark soliton in optical fibers. Phys Rev Lett 1988; 61: 2445–2448.

[82] Hasegawa A, Matsumoto M. Optical Solitons in Fibers. Springer, 2003.

[83] Rosanov NN. Spatial Hysteresis and Optical Patterns. NY, USA, Springer, 2002.

[84] Coen S, Tlidi M, Emplit Ph, Haelterman M, Convection versus Dispersion in Optical Bistability. Phys Rev Lett 1999; 83: 2328–2331.

[85] Gentry CM, Zeng X, Popović MA. Tunable coupled-mode dispersion compensation and its application to on-chip resonant four-wave mixing. Opt Lett 2014; 39: 5689–5692.

[86] Brasch V, Herr T, Geiselmann M, et al. Photonic chip based optical frequency comb using soliton induced Cherenkov radiation. arXiv:1410.8598v2 [physics.optics].